Enhanced ion transport in an ether aided super concentrated ionic liquid electrolyte for long-life practical lithium metal battery applications

Urbi Pal,[a] Fangfang Chen,[a,b] Derick Gyabang,[a] Thushan Pathirana Senadhi,[a] Binayak Roy,[c] Robert Kerr[a], Douglas R. MacFarlane,[b,c] Michel Armand,[a,d] Patrick C. Howlett,[a,b] Maria Forsyth [a,b]*

[a] Institute for Frontier Materials (IFM), Deakin University, Burwood, Victoria 3125, Australia.

[b] ARC Centre of Excellence for Electromaterials Science (ACES), Deakin University, Burwood, Victoria 3125, Australia.

[c] School of Chemistry, Monash University, Clayton 3800, Victoria, Australia.

[d] CIC EnergiGUNE, Parque Tecnológico de Álava, 48, 01510 Miñano, Álava, Spain.

Corresponding Author: * Maria Forsyth

E-mail: maria.forsyth@deakin.edu.au

ABSTRACT: We explore a novel ether aided superconcentrated ionic liquid electrolyte; a combination of ionic liquid, *N*-propyl-*N*-methylpyrrolidinium bis(fluorosulfonyl)imide (C$_3$mpyrFSI) and ether solvent, *1,2* dimethoxy ethane (DME) with 3.2 mol/kg LiFSI salt, which offers an alternative ion-transport mechanism and improves the overall fluidity of the electrolyte. The molecular dynamics (MD) study reveals that the coordination environment of lithium in the ether aided ionic liquid system offers a coexistence of both the ether DME and FSI anion simultaneously and the absence of 'free', uncoordinated DME solvent. These structures lead to very fast kinetics and improved current density for lithium deposition-dissolution processes. Hence the electrolyte is used in a lithium metal battery against a high mass loading (~12 mg/cm^2) LFP cathode which was cycled at a relatively high current rate of 1mA/cm^2 for 350 cycles without capacity fading and offered an overall coulombic efficiency of >99.8 %. Additionally, the rate performance demonstrated that this electrolyte is capable of passing current density as high as 7mA/cm^2 without any electrolytic decomposition and offers a superior capacity retention. We have also demonstrated an 'anode free' LFP-Cu cell which was cycled over 50 cycles and achieved an average coulombic efficiency of 98.74%. The coordination chemistry and (electro)chemical understanding as well as the excellent cycling stability collectively leads toward a breakthrough in realizing the practical applicability of this ether aided ionic liquid electrolytes in lithium metal battery applications, while delivering high energy density in a prototype cell.

Introduction:

The global drive for electric vehicles (EVs) and emerging demands for new applications such as drones, small aircraft and robotics etc., requires urgent development of safe high energy density battery alternatives. The lithium ion battery (LIB) with graphite intercalation anodes was commercialised in the early 1990s; however, their safety, cycle life and more importantly, the overall energy density is limited by the energy density of the anode. Lithium metal is considered as the ultimate anode material for the next generation high energy density batteries, including Li-S and Li-air, since Li metal anodes offer almost ten times higher specific capacity (3860 mAh/g) compared to the current graphite anodes (350 mAh/g) [1]. However, the high reactivity of lithium metal with most electrolytes leads to decomposition followed by extreme passivation of the electrode surface as well as dendrite formation during cycling[2,3]. Thus, new chemistries are required for the design of suitable electrolytes to support lithium metal anode, which is a critical step towards achieving high energy density lithium metal batteries (LMBs).

Another major concern in establishing the high energy density LMB is the choice of cathode material and cathode active material mass loading. In order to maximize the cell level energy density, the commercial-grade LMBs seek to use very high mass loading of cathode active materials (> 10 mg/cm^2) and restrict the thickness of Li metal (~ 50-100 um or less) [4]. However, the higher cathode loading generally leads to a thicker cathode assembly which affects the electrode wetting during electrolyte filling and the ion diffusion path during cell cycling. Additionally, utilising high areal capacity cathodes will necessitate higher cell current densities (to maintain cell charging/discharging times i.e. C-rate) as well as requiring more Li metal to be cycled

at the anode. These factors increase the likelihood of Li dendrite formation and subsequent internal short-circuit and cell failure.

The conventional carbonate based electrolytes that have been optimized for traditional lithium ion batteries (LIBs) have shown poor performance against lithium metal, particularly at high current densities (i.e. high rates of charge/discharge) and thicker cathode assembly for longer term cycling, which leads to subsequent dendrite formation and short-circuits [5,6]. Additionally, the high flammability of organic solvents raises severe safety concerns [2]. In search of a chemically stable and electrochemically superior candidate, electrolytes based on ionic liquids (ILs) have become a subject of great interest due to their superior thermal stability, low vapour pressure and wider electrochemical stability [7]. In particular, the early work of Howlett et al.[8], along with several other researchers[9,10], has demonstrated that ILs and their mixtures show very promising physical and electrochemical properties in lithium metal battery applications. Furthermore, their associated properties can be controlled by various combinations of IL cations and anions as well as the electrolyte compositions [11,12-15,16]. It has also been shown that ultra-high salt concentrations (greater than 50 mol%) in ILs yield electrolytes that provide a high lithium ion transport number and support high charge/discharge rates [10, 17, 18-20]. However, the main challenge in applying high salt concentration ILs in batteries is their high viscosity and poor wettability towards the separator and thicker cathode assemblies [21]. Hence, to realise the global utilization of ILs in high energy density LMBs, one of the effective approaches is to add a co-solvent or diluent to overcome these shortcomings. The nature of the diluent is very crucial; it should enable an improvement in the overall battery performance without compromising the beneficial properties of the ionic liquid. The complex chemistry and speciation in a binary IL electrolyte (i.e. only lithium salt added) has already been extensively discussed in the literature [19, 22-24], however, the solvation structures and

transport properties of 'ternary systems' composed of IL, high salt concentrations and co-solvent have been less explored to date and this is one of the keys to improve lithium ion transport and enable high performance devices. Herein, a detailed and systematic analysis of an ether aided superconcentrated ionic liquid system is reported. The IL, *N*-propyl-*N*-methylpyrrolidinium bis(fluorosulfonyl)imide (C$_3$mpyrFSI) and an organic ether, *1,2* dimethoxyethane (DME) have been combined in varying relative weight percentages, and the resulting electrolyte formed a clear miscible solution. The concentration of lithium bis(fluorosulfonyl)imide (LiFSI) was kept constant at 3.2 mol/kg as the neat C$_3$mpyrFSI IL has a LiFSI salt saturation of 3.2 mol/kg at room temperature [12]. To understand the speciation and solvation environment of the ether aided IL system, the gradual augmentation effect of the DME weight percent in ionic liquid was investigated. After a detailed study of the physical and electro(chemical) properties of the LiFSI/IL/DME ternary electrolyte, an optimum composition was chosen for MD simulation and further investigation in cell configurations including in Li metal/LFP and Cu/LFP with high cathode loading.

Materials and methods

Chemicals

All the chemicals reported here, were of analytical grade. Ionic liquid *N*-propyl-*N*-methylpyrrolidinium bis(fluorosulfonyl)imide (C$_3$mpyrFSI) was purchased from Solvoinic (purity 99.5%). Li-salt of Lithium bis(fluorosulfonyl)imide (LiFSI) was ordered from Solvionic. 1,2 dimethoxyethane (DME) was purchased from Sigma-Aldrich with 99.9% purity and all the materials were kept in an argon filled glove box for further preparation of electrolyte.

Electrolyte preparation

The ionic liquid (IL) was dried under vacuum in Schlenk-line at 50°C for 48 hours before using. The dried IL and DME were mixed in various weight ratios starting from 100:0, 90:10, 80:20, 70:30, 60:40, 50:50 (IL:DME). In all the cases LiFSI was added maintaining the salt concentration to be 3.2 mol/kg. The solutions were allowed to stir at room temperature for 4 hours. As the electrolytes were formulated by weight ratios replacing the IL with ether, hence, these electrolytes are called as 'ether aided ionic liquid electrolytes' in the manuscript. All the prepared ether aided IL electrolytes were kept in argon filled glove box for further characterization and maintaining the electrolyte moisture content <50ppm.

Materials Characterization

Ionic conductivity was performed using MTZ frequency response analyzer between 0.1 Hz to 1MHz and a voltage of 0.1V over a temperature range of -30 °C to 60 °C. A brass block was connected to a thermo-couple for temperature control. The cell constant was calculated using standard 0.01M KCl solution at 25°C and the resistance was determined from the X-axis intercept in the Nyquist plot which was then used to calculate the value of conductivity.

The viscosity was measured using an Anton Paar viscometer using Lovis 2000ME mode. A 10 mm long and 2.5 mm wide diameter capillary was filled with electrolyte and the "rolling ball" method was applied with a constant tilting angle for free falling of the metal ball to measure the viscosity.

A Mettler Toledo DSC1 instrument was used to determine the phase behaviour of the ether aided IL electrolytes, using a heating rate of 10 °C/min and cooling rate of 20 °C/min. The temperature range of the analysis was chosen from -150°C to 60°C with a sample loading of approximately 10 mg. Cyclohexane was analyzed as a reference to calibrate the instrument.

Pulsed-field gradient stimulated echo (PFG-STE) diffusion measurements were performed with a Bruker Avance III 7.05 T spectrometer equipped with a 5 mm Diff50 gradient probe using the gradient pulse time (δ = 2 ms) and the diffusion time (Δ = 25 ms), following the method described by Bayley et al.[25] Samples were filled to a height of 50 mm in a 3 mm (diameter) NMR tube in an argon filled glove box and flame sealed. Then the 3mm tube was immersed in a 5 mm NMR tube containing deuterated water to minimize the convection effect. All measurements were carried out from 10°C to 60°C.

A Perkin Elmer Spectrum 400 was used to record the Fourier transform infrared (FTIR) spectra under an argon atmosphere at room temperature. Sixteen scans from 4000 to 600 cm^{-1} were accumulated per sample.

TGA was performed to understand the thermal decomposition behaviour of the ether aided electrolytes. A Mettler Toledo TGA STARe system was used which operated through automated input and output technology. The crucible was loaded with nearly 10mg of electrolyte and the mass loss was recorded against temperature over a heating range of 25˚C to 535 ˚C with 10˚C/min ramp. The analysis was performed under constant N_2 flow.

Electrochemical measurements

Cyclic voltammetry (CVs) experiments were performed using a Biologic SP200 potentiostat following a conventional three-electrode arrangement where nickel electrode (1.5 mm diameter, ALS Co.) and a platinum wire (APS, 99.95%) were used as working and counter electrodes respectively. The reference electrode was prepared in-house by immersing a silver wire in a solution of C_3mpyrFSI ionic liquid containing 5 mM silver triflate (AgOTf) separated by a glass frit. All the measurements were carried out at room temperature and at 20 mV/sec scan rate. The potentials were calibrated to the ferrocene redox potential after each experiment.

Coin cell fabrication

LFP-Li cells: Commercial lithium iron phosphate (LFP) electrode foils were purchased from CustomCells. Two different mass loadings of LFP cathode were used; a 2 mAh/cm^2 foil with a 12 mg/cm^2 mass loading, and a high capacity 3.5 mAh/cm^2 foil with a mass loading of 21 mg/cm^2. The cathodes were cut into 8 mm diameter discs using an EL-Cell precision hand-held electrode cutter and dried before use. A lithium metal foil of 100 μm thickness (Gelon) was used as the anode (and current collector) for all the battery measurements. CR2032 coin cells (Hohsen Corp.) were used with Celgard 3501 separator. The separator was pre-soaked by the electrolytes (~20 μl) in each case to improve wetting followed by the electrodes wetting (30 μl); hence a total amount of 50 μl electrolyte was used in each Li/LFP cell. Cell cycling was carried out between voltage limits of 2.8 and 3.8 V with one cycle at C/10 (the formation cycle) followed by long-term cycling at C/2 unless mentioned otherwise. The cells were cycled at either 50 ºC or room temperature. Room temperature cycling data is only presented in the electronic supporting information.

LFP-Cu cells: The Copper electrodes (10 mm diameter) were punched and washed with 1 M HCl solution for 2 minutes followed by washing with DI water for 2 minutes and finally with acetone for 2 minutes. The electrodes were vacuum dried for 24 hours at 100 °C and transferred into the glovebox. The cells were assembled with a LFP electrode 3.5 mAh/cm^2 (8 mm diameter) and a Celgard 3501 separator. 50 μl of electrolyte was used in each cell. The first two formation cycles were carried out at C/20 (0.175 mA/cm^2) followed by long-term galvanostatic cycling at C/2 (1.75 mA/cm^2) for 100 cycles at 50 °C between 2.5 – 4.0 V. The formation cycles are shown in the electronic supporting information.

Computational Details:

Results for the neat ionic liquid C$_3$mpyrFSI were taken from our previous work in which the computational details are reported.[26] The 80IL20DME system consisted of 108 C$_3$mpyrFSI ion pairs (IPs), 86 LiFSI ion pairs and 43 DME molecules. All of these molecules are packed in a cubic simulation box randomly using Packmol code.[27] The initial structure was minimized at 393 K and then was equilibrated for 5 ns using the NPT ensemble and the Nose-Hoover and Parrinello-Rahman methods for temperature and pressure coupling. The system was then cooled down to 333 K, 323 K, 313 K, 303 K, 293 K and 293 K, and 5 ns NPT equilibration was run at each temperature, followed by 12 ns NVT run for data collection. The pressure was 1 bar. The electrostatic interaction was computed using Particle-mesh Ewald (PME) methods. The fourier spacing parameter was 0.12 with the 4th order (cubic) interpolation being used. The cut-off distance of 1.2 nm was adopted for both electrostatics and Van der Waals interactions. The C-H bond was constrained. The Velocity Verlet integrator was adopted, with a time step of 1 fs. MD simulations for 80IL20DME system were conducted using GROMACS (version 2016.3).[28] The force field parameters of C$_3$mpyrFSI and lithium ion are taken from CL&P force field.[29]

The parameters for DME are generated using LigParGen online force field generator, which is an OPLS force field parameter generator.[30] The total ion net charge of all cations and anions was scaled down to ± 0.7 in order to account for charge transfer. The atomic charges on the DME molecule are not scaled.

Results and discussion:

Interactions and transport properties

The influence of the ether component on the ionic conductivity of the ether aided IL electrolyte over a wide temperature range (-30 °C to 60 °C) is demonstrated in Figure 1a, where the ionic conductivity increased in electrolytes containing a higher weight percent of DME. The Li-salt concentration was kept constant across all the electrolyte compositions, hence the increasing trend in the ionic conductivity can be attributed to the presence of the ether solvent, DME. To understand the influence of the DME addition, the relative change in ionic conductivity as a function of various compositions is represented at four different temperatures (i.e. -20 °C, 0 °C, 20 °C and 40 °C) in Figure 1b. A prominent upward shift in ionic conductivity is observed when 10 wt% of DME is added to the IL system. Similar increasing trends were observed for all four temperatures. Notably, the relative change in ionic conductivity between electrolytes composed of 60:40 IL:DME and 50:50 IL:DME is less in comparison to the electrolytes composed of lower amounts of DME (90:10, 80:20, IL:DME etc.). This can be correlated to the decrease in the number of total available ionic species with the increased DME mass fraction of the mixtures. The addition of DME also prominently decreased the glass transition temperature (T_g), as demonstrated in Figure 1c which is consistent with the overall increase in ionic conductivity (Figure 1a), as a lower T_g indicates higher mobility in the electrolytes.
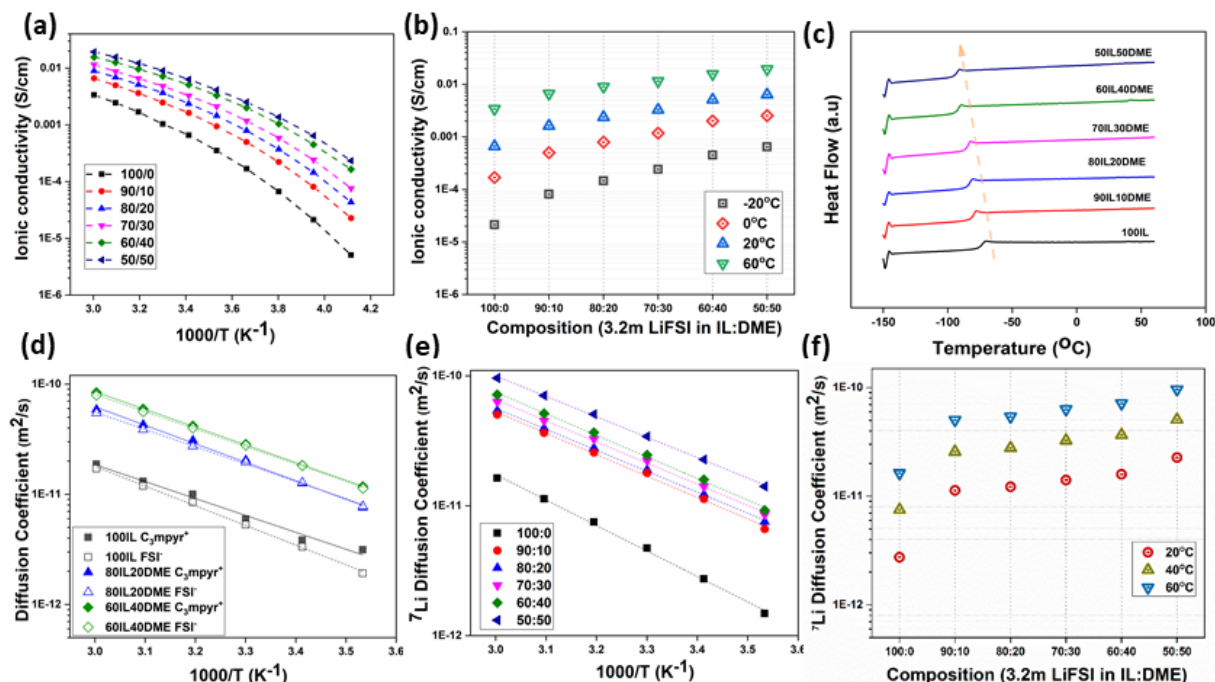
Figure 1: (a) Temperature dependent ionic conductivity for IL:DME electrolytes with 3.2 mol/kg LiFSI; (b) Ionic conductivity as a function of electrolyte composition for different temperatures; -20 °C, 0 °C, 20 °C and 60 °C; (c) DSC traces of the IL:DME electrolytes; (d) Temperature dependent diffusion coefficients for the IL cation and anion in the 100IL, 80IL20DME, 60IL40DME compositions; (e) Temperature dependent diffusion coefficient for Li^+ for IL:DME electrolytes and (f) Li^+ diffusion coefficient as a function of composition at three different temperatures; 20 °C, 40 °C, 60 °C (note: the error bars lay within the markers)

In order to further understand the improved ionic conductivity, measurement of the diffusivity of individual species can provide valuable information. Pulsed field gradient NMR (PFG-NMR) spectroscopy is the most convenient method for this measurement since it can detect and identify individual nuclei that can be attributed to each of the species present in the electrolyte [31, 32]. The diffusivities of the ^1H nuclei (corresponding to C_3mpyr^+) and the ^{19}F nuclei (corresponding to FSI$^-$) are presented in Figure 1d as a function of temperature. For the 100IL electrolyte, the diffusivity of the FSI$^-$ is significantly lower than the C_3mpyr^+ at lower temperatures due to the correlated motions of Li^+ and FSI$^-$ ion aggregates that are normally found in the high salt concentration ILs.

10

In contrast, the anion diffusivity approaches that of the cation at lower temperatures for the 80IL20DME and 60IL40DME electrolytes. This suggests that DME reduces the degree to which the motion of the Li^+ and FSI^- ions are correlated, thereby making the FSI^- motion less encumbered.

Lithium mobility is key for battery performance; the diffusivity of ^7Li in the ether aided IL electrolytes is presented separately in Figure 1e over a wide temperature range. The overall lithium diffusivity increased in electrolytes composed of higher amounts of DME relative to IL, which reflects the trend observed in the ionic conductivity. In Figure 1f, the relative change in lithium diffusivity as a function of composition is presented, which highlights the effect of DME on the Li^+ solvation environment. It shows that the addition of just 10 wt% DME has a prominent effect on the lithium diffusivity, however higher DME doesn't appear to further significantly improve the diffusivity of lithium. This suggests that even a very small amount of DME can have a huge effect on the solvation environment of lithium, which in turn impacts the lithium dynamics.

The Walden plot can be used to establish the relationship between electrolyte conductivity and viscosity. It is a powerful representation which can show the degree of extended ionic interactions by comparing with that of a so-called ideal electrolyte, typically a 1 M (mol/L) aqueous KCl solution [33]. The conductivity and viscosity data are presented in a Walden plot for the 100IL, 80IL20DME and 50IL50DME compositions, giving consideration to three types of electrolyte system; (i) entirely IL based, (ii) an IL dominant composition (where IL weight percentage is higher than DME) and (iii) where the IL and DME weight ratio is the same (Figure 2a). These three compositions show a slightly different deviation from the ideal KCl line but all of them remain within the 90 % dissociation limit. Deviation from the KCl line can indicate the extent of ion correlations [34,35]. Yoon et al.[12] have previously introduced the concept of ion aggregate formation in binary electrolytes with LiFSi in ILs. They reported that the neat IL showed a

deviation from the KCl line, and the deviation was further increased by the gradual addition of LiFSI salt to the IL. This enhanced deviation from the KCl line was attributed to increased ionic association and the formation of ion aggregates of the lithium cation and FSI anion in the ionic liquid. However, the trend was reported to be reversed as the LiFSI concentration approached the saturation point, where the saturated 3.2 mol/kg LiFSI in IL electrolyte again approached the ideal KCl line. This is thought to reflect a changing conduction mechanism which is facilitated by the extended ionic networks in the salt saturated IL system [12]. In the case of the ether aided IL electrolytes studied herein, the addition of DME resulted in a further deviation from the salt saturated IL (100IL) suggesting that addition of DME could lead to a breakdown of the extended ion networks formed by the lithium and anion. This in turn may facilitate an alternate route for a fast ion-exchange mechanism.
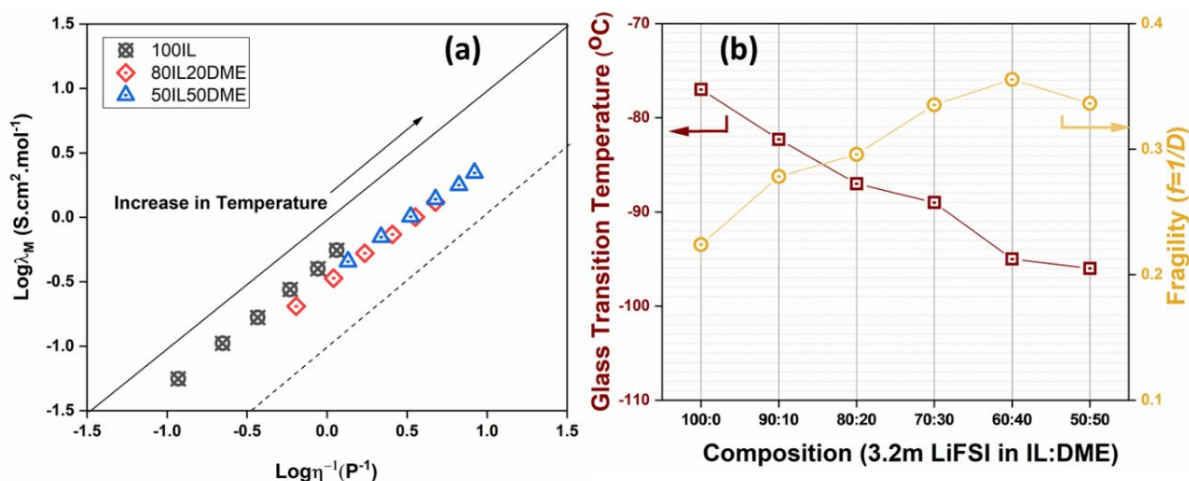

Figure 2: (a) Walden plot for the 100IL, 80IL20DME and 50IL50DME electrolytes, and (b) Comparison of the glass transition (T_g) temperature and fragility as a function of composition (note: the error bars lay within the markers)

The temperature dependence of the ionic conductivity between -30 °C to 60 °C shows a curvature at lower temperatures (Figure 1a) and thus the data were well fitted with the Vogel–Tamman–

Fulcher (VTF) equation [36]. The fitting parameters, i.e. the pseudo-activation energy (B_o), the pre-exponential factor (σ_o) and the ideal glass transition temperature at zero ion mobility (T_o) are given in Table S1. B_o decreases with increased DME content which supports the idea of DME facilitated ion transport. The inverse fragility index, D (where D is equal to 1/f, and where f is fragility), was also calculated and is presented in Figure 2b as a function of electrolyte composition, where fragility is shown to increase with increasing DME content. Fragility defines 'the strength' of a liquid system according to Angell's concept [37]. For example, network forming glasses such as silica are considered strong liquids due to their strong directional bonds which means that, even at T_g, they remain highly viscous whereas a fragile liquid is defined by weaker, less directional bonding. The fragility in the present systems is shown to be increased with increasing DME content, suggesting weaker interionic interactions when DME is added that facilitate easily re-orienting structures in the electrolyte solutions [38]. Interestingly the viscosity is noted to be decreased significantly when DME is introduced into the ionic liquid electrolyte (Figure S1). The 100IL shows a very high viscosity of 450 mPa at 20 °C, whereas 80IL20DME and 50IL50DME electrolytes show lower viscosity of 92 mPa and 45 mPa respectively at 20 °C. The effect of lowering the viscosity agrees well with the increase in the overall ionic conductivity.

The solvation can be also be interrogated with the FTIR spectra represented in Figure 3. The neat IL (without LiFSI salt) shows the -SNS asymmetric stretching frequency (v_a -SNS) at 1100 cm^{-1} however, when 3.2 m LiFSI was added in neat IL (aka, 100IL), the SNS stretching frequency shifted towards higher frequencies. This blue shift indicates a stronger interaction in the solvation of Li$^+$ with the FSI anion [12]. Interestingly, the DME addition in the IL further moves the –SNS stretching towards lower frequencies which indicates a weaker association as well as a change in the coordination environment of Li$^+$. In Figure 3b, both the symmetric and asymmetric stretching

(v_s –SNS and v_a -SNS) are noted to show a red shift which further supports the change in the coordination shell of Li^+. In Figure 3a, a new band corresponding to the stretching of C-O (v -CO) is noted at 1078 cm^{-1} in all the DME containing electrolytes but is absent in neat IL and 100IL. However, the precise nature of the coordination environment for the Li^+ ion in these mixed IL/DME solvent systems is unclear and needs further study.

The strong association of DME within the IL based electrolyte may have a strong influence on thermal stability. The thermo-gravimetric analysis (TGA) was performed for all DME compositions and the thermal degradation presented in Figure S2. The 100IL shows a high thermal stability limit of ~200 °C which is one of the most promising features of IL based electrolytes. However, the onset of evaporation and degradation increased rapidly with higher DME content due to the highly volatile nature of DME. In the case of 20% DME in IL (aka 80IL20DME) an enhanced stability up to 110 °C (compared with 85°C for DME alone) was observed. Hence, in order to maintain the beneficial properties of IL, the optimized hybrid IL/DME electrolyte must contain as minimum as possible DME to obtain the improved transport properties without losing chemical and/or thermal stability provided by the IL.
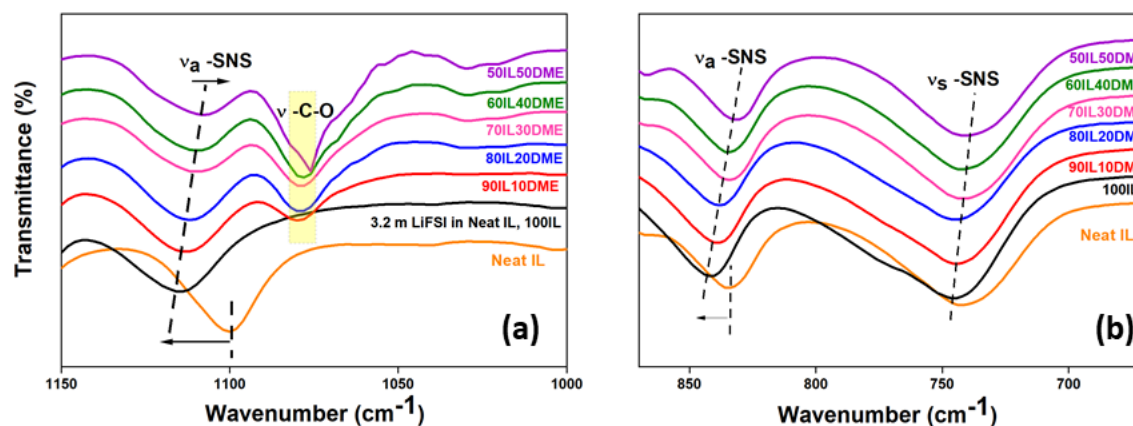
Figure 3: FTIR spectra of the electrolytes, showing the regions centered on (a) the vibration from 1150 cm^{-1} to 1000 cm^{-1} and (b) the vibration from 875 cm^{-1} to 750 cm^{-1}

Electrochemical influence:

The improved ionic conduction, fast lithium mobility and ether induced lithium coordination environment encouraged us to study the ability of these ether aided IL electrolytes to support the electrochemical cycling of lithium metal. Cyclic voltammetry (CV) was used to investigate the lithium deposition-dissolution (or plating and stripping) behavior for the ether aided IL electrolytes. Using the experimental setup shown in Figure 4b, a Ni was used as the working electrode as Ni allows for the deposition of Li metal with little additional overpotential and does not undergo any Li alloying reactions at reductive potentials [39]. Figure 4a presents a comparison of the 1st cycle CVs with varying DME content, whereby the plating and stripping processes are observed for all compositions with varying current-densities. The plating current densities along with the subsequent stripping peak current densities increase with increasing DME content. In Figure 4a, the 100IL electrolyte shows slow lithium plating rate with a broader stripping peak profile. This suggests that despite being highly reversible, the Li redox kinetics are limited by electrolyte mass transport properties, which are dominated by the high viscosity (450 mPaS at 20 ºC). Upon addition of 10 wt% DME (i.e. 90IL10DME), the kinetics are slightly improved with an approximate 20% increase in both deposition rate and peak stripping current-density. However, the addition of a further 20 wt% DME dramatically alleviates the mass transport limitations, facilitating faster Li$^+$ diffusion to/from the electrode surface resulting five-fold increase in the deposition rate and peak stripping current density. The further additions of DME (e.g. 70:30, 60:40 and 50:50 IL:DME) only result in incremental 10-20% improvements. These behaviours can be correlated to the conductivity and ion transport behaviours shown in Figure 1. Figures 4c-4h show

the cycling behavior over the first 10 cycles for each electrolyte composition. Cycling of the Ni working electrode in the 100IL electrolyte shows very stable deposition and stripping behaviors (Figure 4c). The 90IL10DME shows increased plating and stripping current densities, with the total amount (and the fraction of deposited lithium) of Li^+ stripping increasing with each successive cycle (Figure 4d). Interestingly, the 80IL20DME (Figure 4e) undergoes a major five-fold increase in plating current densities while maintaining a high stability over the 10 cycles. The higher DME contents continue to improve on the rate of deposition, however the plating and stripping become increasingly unstable at higher DME contents. This can be attributed to the excess amount of solvent present, most noticeably for the 60/40 and 50/50 IL/DME (Figure 4f and Figure 4g respectively) electrolytes, which can readily react with the freshly plated lithium [40]. These Li metal cycling behaviors indicate that for improved lithium plating-stripping kinetics, a small amount of DME provides better performance compared to higher DME concentrations. Furthermore, even as little as 20% DME can result much better plating stripping current density with faster kinetics at room temperature. Hence, these results indicate that from the range of ether aided ionic liquid electrolyte compositions studied herein, the 80IL0DME electrolyte system appears to possess the most desirable balance between kinetics and stability versus lithium metal, and is selected for further computational modeling and cell cycling studies.
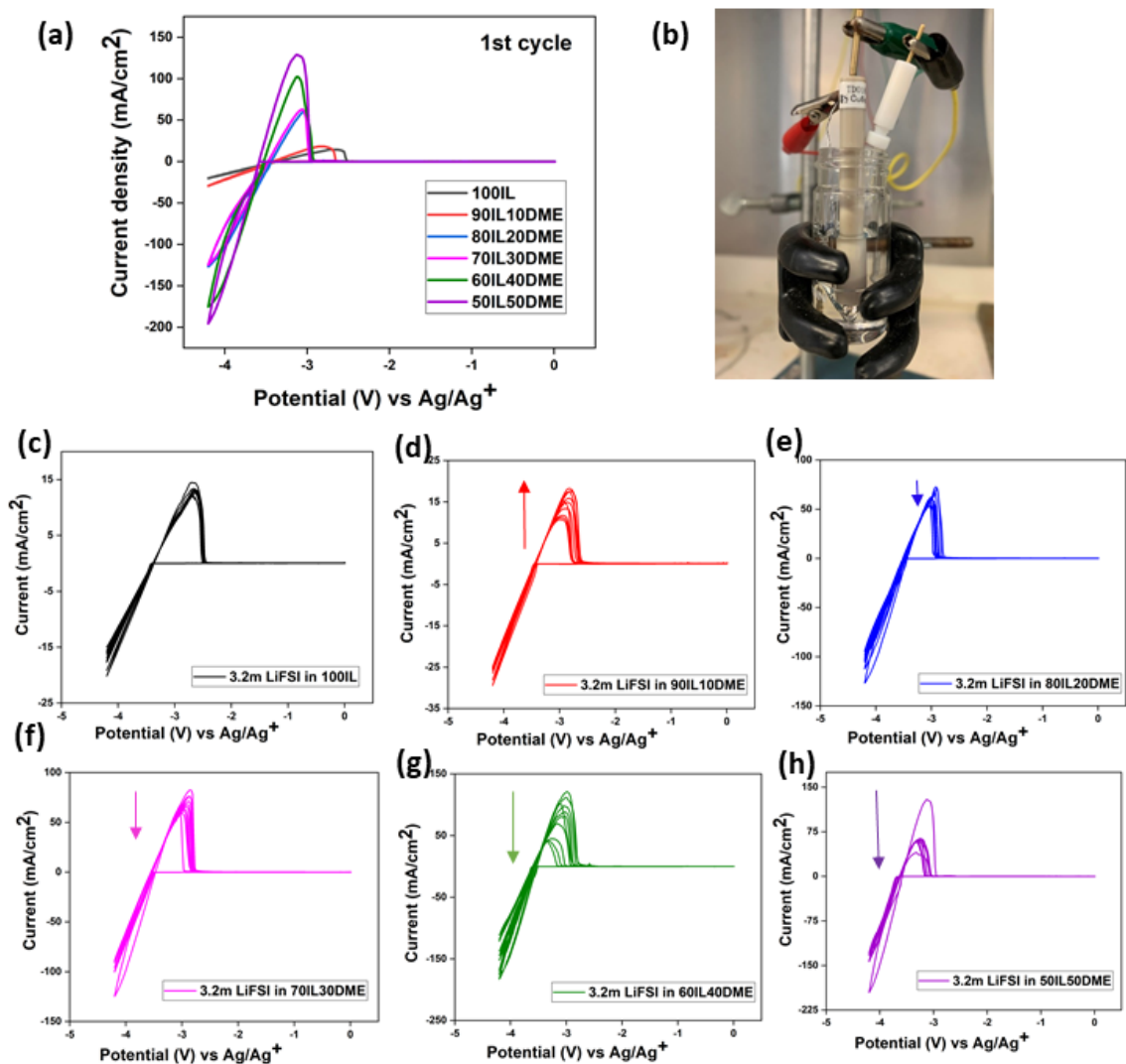
Figure 4: (a) Cyclic voltammograms of a Ni working electrode comparing the 1st cycle in all electrolyte compositions, (b) A photograph of the three electrode setup, (c-h) the first 10 cycles for each electrolyte composition. Scan rate; 20 mV/s.

The coordination environment of lithium by molecular dynamics:

The fundamental understanding in the Li solvation chemistry in ternary system or 'co-solvent aided IL' is very crucial in order to understand the reasons for improved ion dynamics and tailor the conditions for achieving better Li cyclibility. Hence the Li$^+$ coordination structures in the presence of DME, the 80IL20DME system was studied by classic molecular dynamics (MD)

17

simulations and compared with the 100IL system. A snapshot of the Li$^+$ coordination environment, i.e. Li$^+$ ions and their nearest coordination by FSI$^-$ and DME, are shown in Figure 5a.
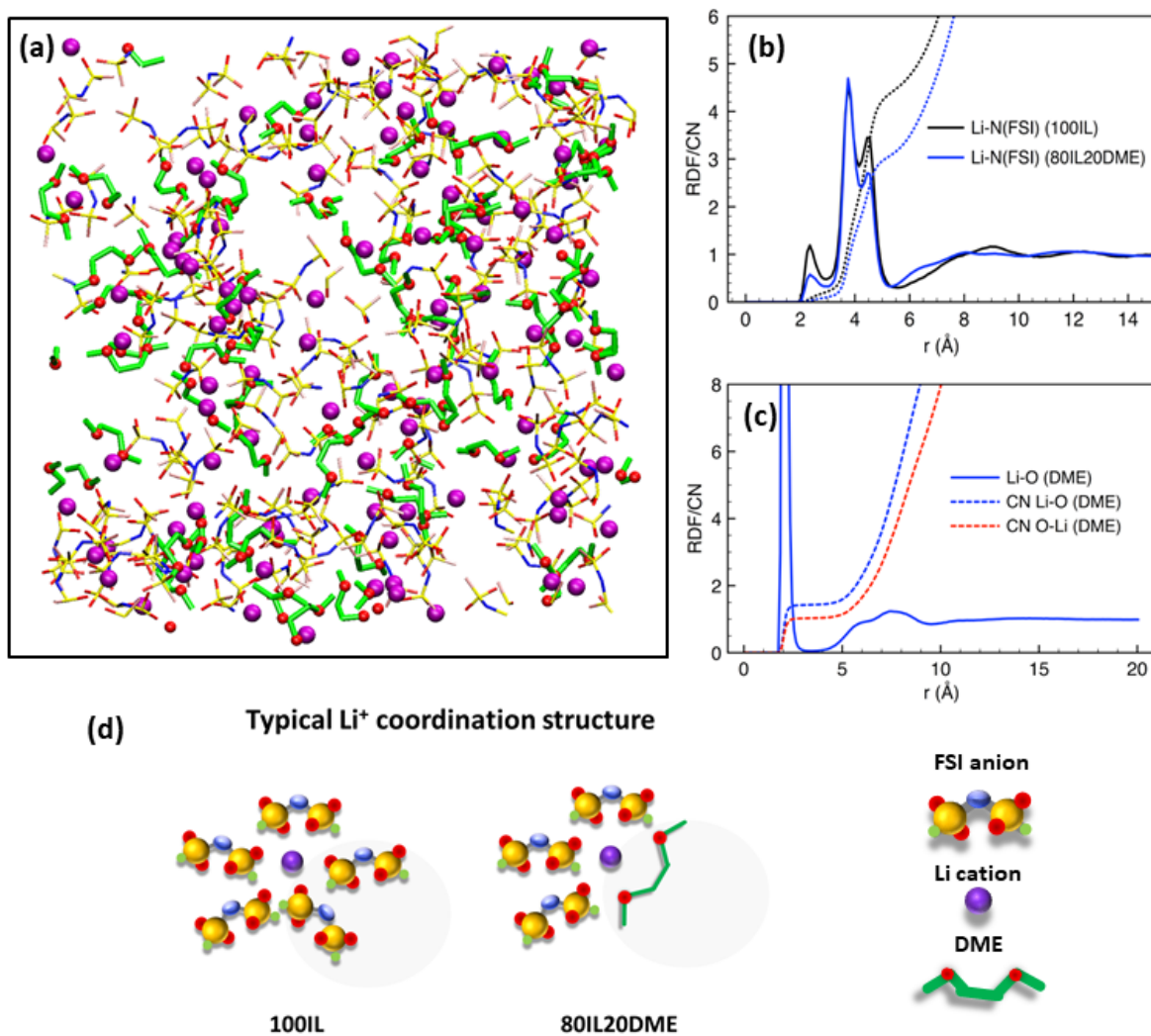
Figure 5: (a) Snapshot of a simulated system showing Li$^+$ ions (purple balls), their coordinated FSI anions (thin yellow sticks) and all DME molecules (bold green sticks) only; (b) Radial distribution function (RDF) of Li-N and their coordination number profiles (dotted lines) for the 100IL and 80Il20DME electrolytes; (c) RDF of Li-O$_{DME}$ (solid lines) and their coordination number profiles (dotted lines). The blue and red dotted lines represent the number of O in Li$^+$ ion's coordination shell and the number of Li$^+$ ions in O's coordination shell, respectively and (d) A schematic representation of a typical Li-coordination environment for the 100IL and 80IL20DME electrolytes

It is important to note that the C$_3$mpyr cations and FSI$^-$ anions that are not coordinating to Li$^+$ are not presented in the snapshot (Figure 5a) in order to clarify the Li$^+$ coordination environment. From this snapshot, it is evident that some Li$^+$ ion coordination structures become hybrid and consist of both FSI$^-$ anions and DME molecules, as expected from the FTIR analysis. The radial distribution function (RDF) and coordination number (CN) between Li$^+$ and the N atom in FSI$^-$ were calculated and are presented in Figure 5b. In the pure IL (100IL), each Li$^+$ coordinates between 4 and 5 FSI$^-$ anions with a CN (Li-N) of 4.5. However, when DME is incorporated into the electrolytes, eg., 80IL20DME, the CN (Li-N) is 3, which suggests that on average, each Li$^+$ coordinates to only 3 FSI$^-$ anions. The RDF for the Li$^+$ and O atom in DME was also calculated and are presented in Figure 5c, with the CN being around 1.4. Considering that there are two oxygen atoms in each DME molecule, this data suggests that there should be some Li$^+$ ions coordinating only to FSI$^-$ (from the snapshot presented this appears to be around 40 % of Li$^+$ ions). Hence, it appears that in the absence of DME (i.e. 100IL), one Li$^+$ coordinates between 4 and 5 FSI$^-$ anions, whereas in the 80IL20DME system, each DME can replace two FSI$^-$ anions resulting in a dominant coordination structure consisting of 2 to 3 FSI$^-$ anions and 1 DME molecule, as illustrated in Figure 5d. This is consistent with the FTIR spectroscopy as the SNS stretching frequency showed a red shift indicating a change in the coordination shell.

Furthermore, we have previously shown that Li^+ and FSI^- form large ion aggregates in the 100IL electrolyte via the sharing of a single FSI^- anion by two Li^+ cations [41]. In order to further study the role of DME in the Li^+ coordination environment, the number of Li^+ cations surrounding each DME oxygen atom, i.e. CN (O_{DME}–Li), was also calculated and found to be equal to 1, as shown in Figure 5c. This suggests that each DME molecule will not act as a bridge between two Li^+ ions (unlike the FSI anions), therefore the extended Li-FSI ion aggregates are disrupted by DME molecules making the Li diffusion mechanism different from that in the 100IL electrolyte (salt saturated IL). Hence from the MD simulations, we can propose that DME works like a lubricant in the aggregated structures (Figure 6) which improve the lithium dynamics. This may also explain the high fragility observed from the VTF behavior since the strong networking usually associated with 'strong' glass formers is broken.
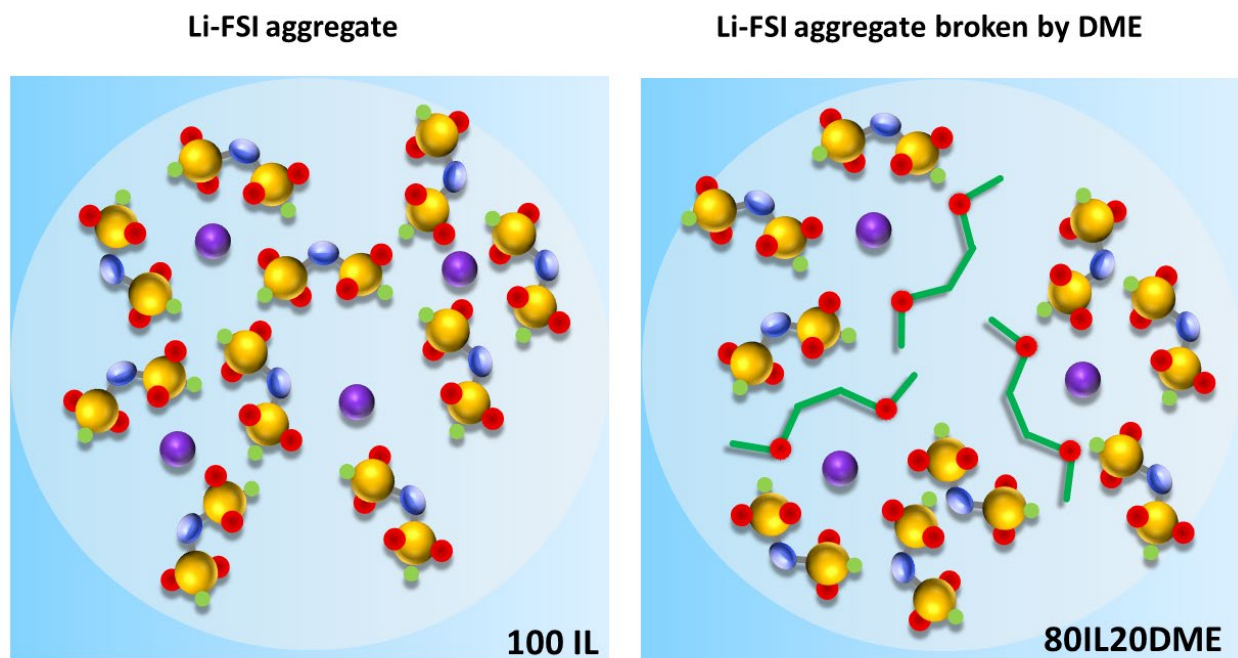

Figure 6: A schematic representation of the effect of DME in breaking down the Li-FSI aggregates, as indicated by MD simulations

Also 80IL20DME does not show the appearance of any free uncoordinated DME molecules, which are more often cited as the reason for poor Li plating stripping efficiency. Therefore, the unavailability of any such uncoordinated DME suggests an improvement in the Li cyclibility, especially under high current density conditions. In order to understand the high current density performance of this electrolyte, in the next section we have studied the application of our electrolyte in a practical high energy density LMB with a high loading commercial cathode.

LFP-Li full cell cycling

In contrast to the traditional Li-ion batteries (LIBs), where graphite is used as an intercalation anode, Li metal batteries (LMBs) utilize Li metal itself as the anode. Replacing graphite with Li metal as the anode achieves a significant increase in specific capacity from 372 mAh/g to 3860 mAh/g. However, a major challenge is to cycle the metallic lithium at higher rates without the formation of dendrites [6]. The conventional organic electrolyte fails to cycle due to the higher parasitic reactions occurring between the electrolyte and lithium metal, leading to a challenge for lithium metal based batteries [6]. Additionally, high temperature provokes rapid degradation of electrolytes over time [42]. Hence higher temperature stability near 50°C is desirable since present devices with organic solvents require active cooling and are rated to well below 50°C. Ionic liquid based electrolytes are known for their high thermal stability but their application in commercial battery is hindered by their ionic conductivity and viscosity related limitations. In this work, our ether aided IL (80IL20DME) offers an improved ionic conductivity (7 mS/cm) and low viscosity (30 mPa) at 50 °C and thermally stable up to 110 °C; hence, here we explore the practical LMB at high current rates at 50 °C. For this study, the olivine structure lithium iron phosphate (LFP) was used as the cathode, owing to its high structural, thermal and electrochemical stability, as reported in literature [43].

Figure 7a presents the long-term cycling using an LFP cathode with an areal capacity of 2 mAh/cm^2 (mass loading ~12 mg/cm^2) against a thin Li metal anode (~ 100μm) where the Li metal was used directly without any chemical modification or passivation. To elucidate the tolerance of the 80IL20DME electrolyte to the prolonged cycling, the LFP-Li cell was cycled at a current density of 1 mA/cm^2 where it delivers the full areal capacity of 2 mAh/cm^2 (or ~170 mAh/g) for 350 cycles without any capacity decay or cell failure. Figure 7a also shows the coulombic efficiency of > 99.8 %, which proves that the electrolyte is capable of sustaining fast charge and discharge without continuous and excessive electrolyte degradation. Previous work by Bai et al. reported that, with a standard commercial organic electrolyte formulation (1 M LiPF$_6$ in EC/EMC/DMC = 1/1/1 (v/v/v)), a capacity retention of 69% with an average Coulombic efficiency of 95% after 300 cycles was demonstrated using a Li-LFP (LFP loading ~10.45 mg/cm^2) full cell. They improved the cycling efficiency by using rGO-coated Li metal [44]. There have been numerous recent reports on ways in which to improve on the poor cycle stability of bare lithium metal via e.g. chemical electrode pre-treatments and electrode surface modifications. Some of the more notable approaches which have been demonstrated through high capacity full cell performance have been captured in Table 1. Our electrolyte has successfully demonstrated cell cycling performances that are equal to or superior than many of these results, despite the use of bare lithium metal. The ability to cycle without any capacity decay which primarily indicates the superiority of ionic liquid chemistry with lithium metal which can protect the metal surface without any short-circuit during cycling. Figure 7b shows the evolution of the voltage profile of the LFP-Li cell which exhibits remarkably stable behavior over the 350 cycles. Cell cycling at 20 ºC was also carried out (Figure S4) and shows a similar stable performance.
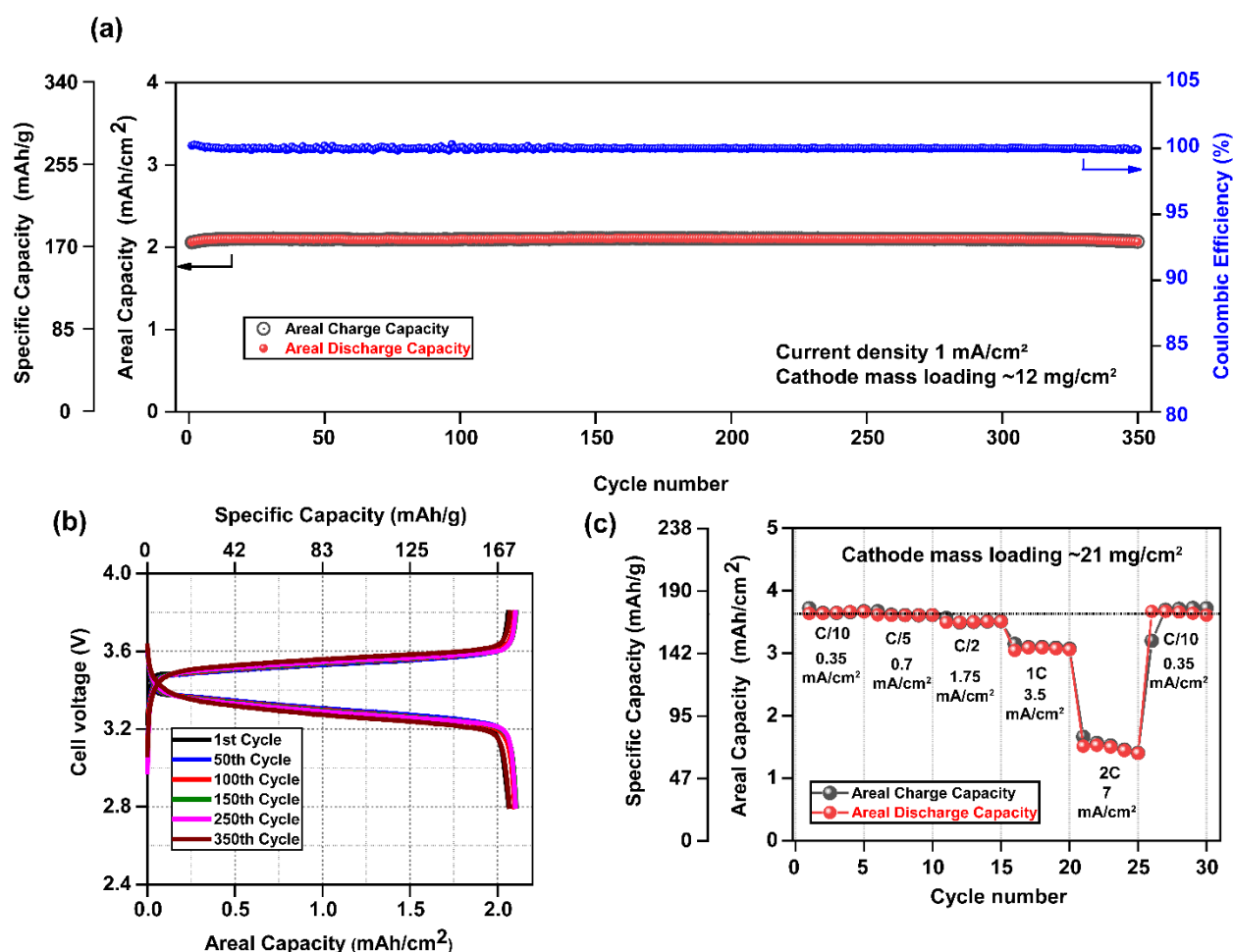
Figure 7: a) Long-term galvanostatic cycling at 1 mA/cm² of the LFP-Li cell prepared using the 80IL20DME electrolyte and a 2 mAh/cm² (nominal) commercial LFP cathode; (b) Evolution of the cell charge/discharge voltage profiles during the galvanostatic cycling in (a). (c) Rate capability test of a high capacity LFP-Li cell prepared using a 3.5 mAh/cm² (nominal) LFP cathode. All cell cycling was performed at 50 °C.

In Figure 7c, we have used even thicker LFP cathode assembly where the active material mass loading is ~21 mg/cm². This is one of the highest reported cathode loadings in LFP-Li cell applications, offering an areal capacity of 3.5 mAh/cm². The rate capability test was performed at different current densities and the corresponding capacities were recorded. The areal capacity remains stable (~ 3.4 - 3.6 mAh/cm²) up to 1.75 mA/cm² (C/2). When the current density is increased to 3.5 mA/cm² (1C), the areal capacity drops to 3 mAh/cm² and then again to ~ 1.5

mAh/cm^2 at 7 mA/cm^2 (2C). Full capacity is regained when the rate is subsequently returned to 0.35 mA/cm^2, demonstrating stability of the cell after cycling at high rates. The retention of the discharge capacity up to practical current densities of 1.75 mA/cm^2 is a benchmark result in the field of LMBs and demonstrates the superior reversibility and excellent tolerance to high-rate cycling for the 80IL20DME electrolyte. The stable long-term performance is also a key measure of the excellent ability of the ether aided electrolyte to effectively cycle the high loading LFP cathode as well as facilitate active lithium metal cycling on the anode side without the formation of dendrites or short circuit-induced failure. The preparation of pouch cells for further analysis and testing with this high LFP cathode loading is currently underway in our laboratory.

Table 1: Comparison of lithium metal battery (LMB) performance using various organic electrolytes vs our developed electrolyte

Electrolyte	Cell configuration	Li thickness	Cycle number and current rate	Coulombic efficiency	Initial and final capacity	Capacity retention	Ref
1 M LiPF$_6$ in 1:1 (V/V) EC/DMC	LFP/ bare Li metal Cathode mass loading ~6.8 mg, theoretical areal capacity 1.04 mAh/cm^2	150 μm	150 cycles, 1C (1 mA/cm^2)	NR	150 mAh/g, 115 mAh/g	63%	Hu et al., [45] Chemistry of Materials, ACS, 2017
	LFP/Li with **LiNO$_3$**			NR	150 mAh/g, 131 mAh/g	92%	
	LFP/Li with **polyethyl α-cyanoacrylate(PECA)+LiNO$_3$**			NR	150 mAh/g, 148 mAh/g	97%	
1 M LiPF$_6$ in EC, EMC, and DMC (1:1:1 v/v/v)	LFP/ bare Li metal Cathode mass loading ~10.45 mg/cm^2	NR	300 cycles, 1C (1.8 mA/cm^2)	~96%	129.8 mAh/g, 89.5 mAh/g	69%	Bai et al, [44] Advanced Materials,

Electrolyte	Cell	Thickness	Cycles, Rate	CE	Capacity	Retention	Reference
	LFP/ **rGO coated** Li	NR		~99.8%	130.1 mAh/g, 128.8 mAh/cm2	99%	Wiley, 2018
1 M LiTFSI, DME/DOL (1/1, v/v) and **2 wt% LiNO$_3$**	LFP/Li Cathode mass loading ~4.5 mg/cm^2	NR	400 cycles, 0.1C (0.08 mA/cm^2)	98.88%	140 mAh/g, 120 mAh/g	86%	Assegie et al., [46] Nanoscale, RSC, 2018
1 M LiPF$_6$ in 1:1 (V/V) EC/DEC	LFP/ Li Cathode mass loading ~7.4 mg/cm^2	590 µm	350 cycles, 2C (2.5 mA/cm^2)	NR	120 mAh/g, 60 mAh/g	50%	Tang et al, [47] Advanced Materials, Wiley, 2018
	LFP/ 330nm Li$_x$Si			99.7	140 mAh/g, ~140 mAh/g	~100%	
1 M LiPF$_6$ in 1:1:1 EC/PC/DEC with **10% fluoroethylene carbonate (FEC) and 1% vinylene carbonate (VC).**	(i)LFP/Li Cathode mass loading ~5 mg/cm^2	NR	500 cycles, 5C (4.25 mA/cm^2)	~100%	125 mAh/g, 77.5 mAh/g	62%	Wan et al, [48] Nature Comm, 2020
	(ii)LFP/Li$_{22}$Sn$_5$	500 µm		~100%	132 mAh/g, 120 mAh/g	91%	
1 M LiPF$_6$ in EC, DEC, DMC) in a volume ratio of 1 : 1 : 1	LFP/ Li Cathode mass loading ~5.5 mg/cm^2	450 µm	100 cycles, C/5 (0.19 mA/cm^2)	~95%	160 mAh/g, 145 mAh/g	90.6%	Yao et al., [49] JMCA, 2019
	LFP/ rGO coated Li			99.1%	160 mAh/g, 159 mAh/g	99.3%	
3.2 m LiFSI in 80/20 C$_3$mpyrFSI/DME (wt/wt)	LFP/ Bare Li Cathode mass loading ~12 mg/cm^2	100 µm	350 cycles, C/2, (1 mA/cm^2)	> 99.8%	170 mAh/g, 169 mAh/g	99.4%	This work

Cells shaded in green indicate where bare Li metal was used.

NR = Not Reported.

'Anode free' LFP-Cu cell cycling

A prominent recent trend in Li metal battery chemistry is to assess the electrolyte performance in the presence of 'zero' excess lithium metal, as excess Li metal can artificially maintain a high coulombic efficiency which could produce an inflated value [50]. In such cases, the most appropriate method to evaluate the cell performance is where only the current collector (most commonly Cu substrate) is used as an anode in the absence of an actual Li metal anode, hence refered to as 'anode-free' cell configuration. As there is no 'active' lithium source at the anode side, the coulombic efficiency measures the ratio between the amount of the deposited lithium from the cathode side to the current collector (i.e., charge capacity) and the amount of stripped lithium after dissolution (i.e., discharge capacity). However, the nucleation and growth of the Li deposit can be largely influenced by the choice of current collector [51]. Herein, we have explored the ability of the ether aided IL electrolyte to perform in the anode free cell configuration with a thick LFP electrode (which corresponds to an areal capacity of 3.5 mAh/cm^2) and a Cu current collector. This is one of the highest areal capacity LFP electrodes used in 'anode-free' lithium metal studies reported to date in the literature. Figure 8a demonstrates the long term cycling of LFP-Cu cells and their coulombic efficiency at a practical level current density of 1.75 mA/cm^2 over 50 cycles. Figure 8b shows the corresponding voltage profile for a different number of cycles, where the voltage hysteresis was stable throughout cycling and shows a capacity retention of 47.7% after 50 cycles. Previously, Qian et al[50] reported the capacity retention largely depended on the charge and discharge current rates. They proposed a slow rate of charge (0.2 mA/cm^2) and fast rate of discharge current density (2 mA/cm^2) which resulted in higher coulombic efficiency and capacity retention when they used a lesser areal capacity (1.7 mAh/cm^2) LFP cathode [50]. However, at the same charge and discharge rate (i.e. 2 mA/cm^2 for both steps), a capacity retention of ~45% was

achieved after 50 cycles using 4 M LiFSI in DME electrolyte. Very recently, Nilsson et al.[52] studied even higher LFP areal loading cathodes (3.5 mAh/cm^2) for anode free cells which is very similar to our cathode configuration. They reported that with a carbonate based organic electrolyte (1.86 M LiTFSI in EC), the LFP Cu cell was stable up to 30 cycles and the first discharge capacity was found ~2.7 mAh/cm^2 with 87% coulombic efficiency at a current density of 1 mA/cm^2. In the present work, the charge and discharge capacities for the first cycle (i.e. the formation cycle, Figure S5) are 3.7 mAh/cm^2 and 3.3 mAh/cm^2, respectively, with a coulombic efficiency of 89.0 %. This is an effective measure of the superiority of the ether aided ionic liquid electrolyte over the organic electrolytes in this configuration. In another study, Nanda et al. introduced a parameter called the lithium inventory retention rate (LIRR), which is analogous to coulombic efficiency and can be used to compare across different studies based on capacity retention for anode-free cells [53]. Based on this method, we calculated a LIRR of 98.69% including the formation cycles and 98.72% without the formation cycles and compared with the literature in Table S3. These values are amongst the very best reported to date and signifies that this ether aided IL electrolyte can serve as a promising electrolyte for next generation high energy density lithium metal batteries.
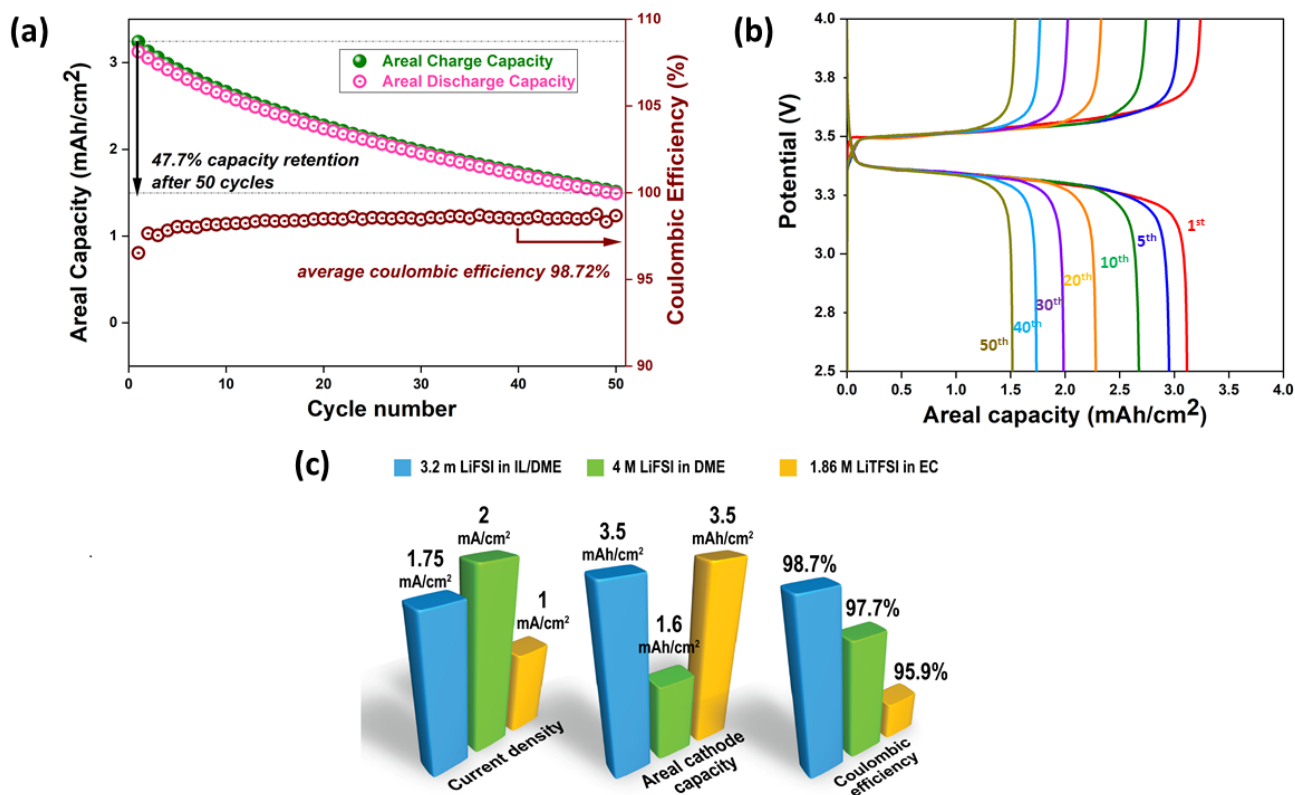
Figure 8: a) Capacity retention and coulombic efficiency during galvanostatic cycling at 1.75 mA/cm^2 (C/2) of an anode-free LFP-Cu cell using a 3.5 mAh/cm^2 (nominal) LFP cathode and 80IL20DME electrolyte. (b) Evolution of the cell voltage profile from (a). (c) A comparison of our electrolyte performance and testing conditions with two prominent electrolytes found in literature (see Table 1 for more information).

Conclusion

Several key aspects relating to the electrolyte performance for application in LMBs have been investigated for a highly concentrated, ether aided IL electrolyte. An enhancement in the overall ionic conductivity and a decrease in the viscosity was observed when DME was added to the IL electrolyte. A 20% DME addition was found to give the best balance of improved transport properties and electrochemical cycling stability where DME acted as a lubricant in the solvation

environment to improve Li^+ transport. From the MD simulation study on the lithium coordination environment, we can state that the addition of DME to a highly concentrated IL based electrolyte offers a 'fast exchange environment' for lithium, which has a prominent effect on the electrochemical plating and stripping of lithium. A practical high current rate of 1 mA/cm^2 was applied to a high cathode loading of LFP/Li cell which successfully cycled over 350 cycles with an overall coulombic efficiency of >99.8 %. The rate performance also demonstrated that this electrolyte supports current densities as high as 7 mA/cm^2 without any significant electrolytic decomposition or short circuiting. Cycling in a LFP-Cu cell configuration, this electrolyte achieved a 98.7% average coulombic efficiency for 50 cycles, a promising result to enable anode free cells. This work is a significant step towards the breakthrough in realizing a practical, high specific energy lithium metal battery where our novel ether aided IL can serve as an electrolyte for stable, long life lithium battery performance. Future work around the detailed characterisation of the Li metal morphology evolution and the electrode-electrolyte interphase is currently underway, in addition to further cell cycling studies using pouch cell format.

- **ASSOCIATED CONTENT**

Supporting Information. The following files are available free of charge.

VTF fitting parameters, Viscosity, Thermo-gravimetric analysis (TGA), RDF of Li-N (FSI) at different temperatures, room temperature LFP-Li cycling, the voltage profile of formation cycle of LFP-Cu cell, Long term cycling of LFP-Cu cell over 100 cycle.

- **AUTHOR INFORMATION**

Corresponding Author

*Maria Forsyth

Tel: +61392446818

Email: maria.forsyth@deakin.edu.au

Twitter: https://twitter.com/professormaria

Group website: https://www.deakin.edu.au/about-deakin/people/maria-forsyth

- **NOTES:**

The authors declare no competing financial interest.

- **ACKNOWLEDGMENTS:**

- **REFERENCES:**

1.   Tarascon, J. M.; Armand, M., Issues and challenges facing rechargeable lithium batteries. *Nature* **2001,** *414* (6861), 359-367.

2.   Xu, K., Electrolytes and Interphases in Li-Ion Batteries and Beyond. *Chemical Reviews* **2014,** *114* (23), 11503-11618.

3.   Aurbach, D.; Zinigrad, E.; Cohen, Y.; Teller, H., A short review of failure mechanisms of lithium metal and lithiated graphite anodes in liquid electrolyte solutions. *Solid State Ionics* **2002,** *148* (3), 405-416.

4.   Chen, S.; Niu, C.; Lee, H.; Li, Q.; Yu, L.; Xu, W.; Zhang, J.-G.; Dufek, E. J.; Whittingham, M. S.; Meng, S.; Xiao, J.; Liu, J., Critical Parameters for Evaluating Coin Cells and Pouch Cells of Rechargeable Li-Metal Batteries. *Joule* **2019,** *3* (4), 1094-1105.

5.   Aurbach, D., The Study of Electrolyte Solutions Based on Ethylene and Diethyl Carbonates for Rechargeable Li Batteries. *Journal of The Electrochemical Society* **1995,** *142* (9), 2882.

6.   Lu, D.; Shao, Y.; Lozano, T.; Bennett, W. D.; Graff, G. L.; Polzin, B.; Zhang, J.; Engelhard, M. H.; Saenz, N. T.; Henderson, W. A.; Bhattacharya, P.; Liu, J.; Xiao, J., Failure Mechanism for Fast-Charged Lithium Metal Batteries with Liquid Electrolytes. *Advanced Energy Materials* **2015,** *5* (3).

7.   Armand, M.; Endres, F.; MacFarlane, D. R.; Ohno, H.; Scrosati, B., Ionic-liquid materials for the electrochemical challenges of the future. *Nature Materials* **2009,** *8* (8), 621-629.

8.   Howlett, P. C.; MacFarlane, D. R.; Hollenkamp, A. F., High Lithium Metal Cycling Efficiency in a Room-Temperature Ionic Liquid. *Electrochemical and Solid-State Letters* **2004,** *7* (5), A97.

9.   Matsumoto, H.; Sakaebe, H.; Tatsumi, K.; Kikuta, M.; Ishiko, E.; Kono, M., Fast cycling of Li/LiCoO2 cell with low-viscosity ionic liquids based on bis(fluorosulfonyl)imide [FSI]−. *Journal of Power Sources* **2006,** *160* (2), 1308-1313.

10.   Yoon, H.; Howlett, P. C.; Best, A. S.; Forsyth, M.; MacFarlane, D. R., Fast Charge/Discharge of Li Metal Batteries Using an Ionic Liquid Electrolyte. *Journal of The Electrochemical Society* **2013,** *160* (10), A1629-A1637.

11.   Jeong, S.; Li, S.; Appetecchi, G. B.; Passerini, S., Asymmetric ammonium-based ionic liquids as electrolyte components for safer, high-energy, electrochemical storage devices. *Energy Storage Materials* **2019,** *18*, 1-9.

12.   Yoon, H.; Best, A. S.; Forsyth, M.; MacFarlane, D. R.; Howlett, P. C., Physical properties of high Li-ion content N-propyl-N-methylpyrrolidinium bis(fluorosulfonyl)imide based ionic liquid electrolytes. *Physical Chemistry Chemical Physics* **2015,** *17* (6), 4656-4663.

13.   Girard, G. M. A.; Hilder, M.; Nucciarone, D.; Whitbread, K.; Zavorine, S.; Moser, M.; Forsyth, M.; MacFarlane, D. R.; Howlett, P. C., Role of Li Concentration and the SEI Layer in Enabling High Performance Li Metal Electrodes Using a Phosphonium Bis(fluorosulfonyl)imide Ionic Liquid. *The Journal of Physical Chemistry C* **2017,** *121* (39), 21087-21095.

14.   MacFarlane, D. R.; Forsyth, M.; Howlett, P. C.; Kar, M.; Passerini, S.; Pringle, J. M.; Ohno, H.; Watanabe, M.; Yan, F.; Zheng, W.; Zhang, S.; Zhang, J., Ionic liquids and their solid-state analogues as materials for energy generation and storage. *Nature Reviews Materials* **2016,** *1* (2), 15005.

15.   Makhlooghiazad, F.; Guazzagaloppa, J.; O'Dell, L. A.; Yunis, R.; Basile, A.; Howlett, P. C.; Forsyth, M., The influence of the size and symmetry of cations and anions on the physicochemical behavior of organic ionic plastic crystal electrolytes mixed with sodium salts. *Physical Chemistry Chemical Physics* **2018,** *20* (7), 4721-4731.

16.   Yang, H.; Hwang, J.; Wang, Y.; Matsumoto, K.; Hagiwara, R., N-Ethyl-N-propylpyrrolidinium Bis(fluorosulfonyl)amide Ionic Liquid Electrolytes for Sodium Secondary Batteries: Effects of Na Ion Concentration. *The Journal of Physical Chemistry C* **2019,** *123* (36), 22018-22026.

17.   Kerr, R.; Singh, N.; Arthur, T. S.; Pathirana, T.; Mizuno, F.; Takechi, K.; Forsyth, M.; Howlett, P. C., Water-tolerant lithium metal cycling in high lithium concentration phosphonium-based ionic liquid electrolytes. *Sustainable Energy & Fuels* **2018,** *2* (10), 2276-2283.

18.   Girard, G. M. A.; Hilder, M.; Zhu, H.; Nucciarone, D.; Whitbread, K.; Zavorine, S.; Moser, M.; Forsyth, M.; MacFarlane, D. R.; Howlett, P. C., Electrochemical and physicochemical properties of small phosphonium cation ionic liquid electrolytes with high lithium salt content. *Physical Chemistry Chemical Physics* **2015,** *17* (14), 8706-8713.

19.   Yamada, Y.; Yamada, A., Review—Superconcentrated Electrolytes for Lithium Batteries. *Journal of The Electrochemical Society* **2015,** *162* (14), A2406-A2423.

20.   Pal, U.; Girard, G. M. A.; O'Dell, L. A.; Roy, B.; Wang, X.; Armand, M.; MacFarlane, D. R.; Howlett, P. C.; Forsyth, M., Improved Li-Ion Transport by DME Chelation in a Novel Ionic Liquid-Based Hybrid Electrolyte for Li–S Battery Application. *The Journal of Physical Chemistry C* **2018,** *122* (26), 14373-14382.

21.   Eftekharnia, M.; Hasanpoor, M.; Forsyth, M.; Kerr, R.; Howlett, P. C., Toward Practical Li Metal Batteries: Importance of Separator Compatibility Using Ionic Liquid Electrolytes. *ACS Applied Energy Materials* **2019,** *2* (9), 6655-6663.

22.   Forsyth, M.; Yoon, H.; Chen, F.; Zhu, H.; MacFarlane, D. R.; Armand, M.; Howlett, P. C., Novel Na+ Ion Diffusion Mechanism in Mixed Organic–Inorganic Ionic Liquid Electrolyte Leading to High Na+ Transference Number and Stable, High Rate Electrochemical Cycling of Sodium Cells. *The Journal of Physical Chemistry C* **2016,** *120* (8), 4276-4286.

23.   Wilken, S.; Xiong, S.; Scheers, J.; Jacobsson, P.; Johansson, P., Ionic liquids in lithium battery electrolytes: Composition versus safety and physical properties. *Journal of Power Sources* **2015,** *275*, 935-942.

24.   Dagousset, L.; Nguyen, G. T. M.; Vidal, F.; Galindo, C.; Aubert, P.-H., Ionic liquids and γ-butyrolactone mixtures as electrolytes for supercapacitors operating over extended temperature ranges. *RSC Advances* **2015,** *5* (17), 13095-13101.

25.   Bayley, P. M.; Lane, G. H.; Rocher, N. M.; Clare, B. R.; Best, A. S.; MacFarlane, D. R.; Forsyth, M., Transport properties of ionic liquid electrolytes with organic diluents. *Physical Chemistry Chemical Physics* **2009,** *11* (33), 7202-7208.

26.   Martin, P.-A.; Chen, F.; Forsyth, M.; Deschamps, M.; O'Dell, L. A., Correlating Intermolecular Cross-Relaxation Rates with Distances and Coordination Numbers in Ionic Liquids. *The Journal of Physical Chemistry Letters* **2018,** *9* (24), 7072-7078.

27.   Martínez, L.; Andrade, R.; Birgin, E. G.; Martínez, J. M., PACKMOL: A package for building initial configurations for molecular dynamics simulations. *J. Comput. Chem.* **2009,** *30* (13), 2157-2164.

28.   Lindahl, E.; Hess, B.; van der Spoel, D., GROMACS 3.0: a package for molecular simulation and trajectory analysis. *Molecular modeling annual* **2001,** *7* (8), 306-317.

29.   Canongia Lopes, J. N.; Pádua, A. A. H., CL&P: A generic and systematic force field for ionic liquids modeling. *Theoretical Chemistry Accounts* **2012,** *131* (3), 1129.

30.   Dodda, L. S.; Cabeza de Vaca, I.; Tirado-Rives, J.; Jorgensen, W. L., LigParGen web server: an automatic OPLS-AA parameter generator for organic ligands. *Nucleic Acids Research* **2017,** *45* (W1), W331-W336.

31.   Cohen, Y.; Avram, L.; Frish, L., Diffusion NMR spectroscopy in supramolecular and combinatorial chemistry: an old parameter--new insights. *Angew Chem Int Ed Engl* **2005,** *44* (4), 520-54.

32.   Simons, T. J.; Bayley, P. M.; Zhang, Z.; Howlett, P. C.; MacFarlane, D. R.; Madsen, L. A.; Forsyth, M., Influence of Zn2+ and Water on the Transport Properties of a Pyrrolidinium Dicyanamide Ionic Liquid. *The Journal of Physical Chemistry B* **2014,** *118* (18), 4895-4905.

33.   Angell, C. A.; Byrne, N.; Belieres, J.-P., Parallel Developments in Aprotic and Protic Ionic Liquids: Physical Chemistry and Applications. *Accounts of Chemical Research* **2007,** *40* (11), 1228-1236.

34.   MacFarlane, D. R.; Chong, A. L.; Forsyth, M.; Kar, M.; Vijayaraghavan, R.; Somers, A.; Pringle, J. M., New dimensions in salt-solvent mixtures: a 4th evolution of ionic liquids. *Faraday Discuss* **2017,** *206*, 9-28.

35.   MacFarlane, D. R.; Forsyth, M.; Izgorodina, E. I.; Abbott, A. P.; Annat, G.; Fraser, K., On the concept of ionicity in ionic liquids. *Phys Chem Chem Phys* **2009,** *11* (25), 4962-7.

36.   Angell, C. A., On the Importance of the Metastable Liquid State and Glass Transition Phenomenon to Transport and Structure Studies in Ionic Liquids. I. Transport Properties1. *The Journal of Physical Chemistry* **1966,** *70* (9), 2793-2803.

37.   Böhmer, R.; Ngai, K. L.; Angell, C. A.; Plazek, D. J., Nonexponential relaxations in strong and fragile glass formers. *The Journal of Chemical Physics* **1993,** *99* (5), 4201-4209.

38.   Hartl, R.; Fleischmann, M.; Gschwind, R. M.; Winter, M.; Gores, H. J., A Liquid Inorganic Electrolyte Showing an Unusually High Lithium Ion Transference Number: A Concentrated Solution of LiAlCl4 in Sulfur Dioxide. *Energies* **2013,** *6* (9).

39.   Wibowo, R.; Ward Jones, S. E.; Compton, R. G., Kinetic and Thermodynamic Parameters of the Li/Li+ Couple in the Room Temperature Ionic Liquid N-Butyl-N-methylpyrrolidinium Bis(trifluoromethylsulfonyl) Imide in the Temperature Range 298−318 K: A Theoretical and Experimental Study Using Pt and Ni Electrodes. *The Journal of Physical Chemistry B* **2009,** *113* (36), 12293-12298.

40.   Qian, J.; Henderson, W. A.; Xu, W.; Bhattacharya, P.; Engelhard, M.; Borodin, O.; Zhang, J. G., High rate and stable cycling of lithium metal anode. *Nat Commun* **2015,** *6*, 6362.

41.   Chen, F.; Howlett, P.; Forsyth, M., Na-Ion Solvation and High Transference Number in Superconcentrated Ionic Liquid Electrolytes: A Theoretical Approach. *The Journal of Physical Chemistry C* **2018,** *122* (1), 105-114.

42.   Leng, F.; Tan, C. M.; Pecht, M., Effect of Temperature on the Aging rate of Li Ion Battery Operating above Room Temperature. *Scientific Reports* **2015,** *5* (1), 12967.

43.   John, M. A.; B. Goodenough, A.; Masquelier;, A. K. P. K. S. N. C., CATHODE MATERIALS FOR SECONDARY (RECHARGEABLE) LITHIUM BATTERIES *US Patent 6,514,640 B1* **2003**.

44.   Bai, M.; Xie, K.; Yuan, K.; Zhang, K.; Li, N.; Shen, C.; Lai, Y.; Vajtai, R.; Ajayan, P.; Wei, B., A Scalable Approach to Dendrite-Free Lithium Anodes via Spontaneous Reduction of Spray-Coated Graphene Oxide Layers. *Adv Mater* **2018**, e1801213.

45.   Hu, Z.; Zhang, S.; Dong, S.; Li, W.; Li, H.; Cui, G.; Chen, L., Poly(ethyl α-cyanoacrylate)-Based Artificial Solid Electrolyte Interphase Layer for Enhanced Interface Stability of Li Metal Anodes. *Chemistry of Materials* **2017,** *29* (11), 4682-4689.

46.   Assegie, A. A.; Cheng, J. H.; Kuo, L. M.; Su, W. N.; Hwang, B. J., Polyethylene oxide film coating enhances lithium cycling efficiency of an anode-free lithium-metal battery. *Nanoscale* **2018,** *10* (13), 6125-6138.

47.   Tang, W.; Yin, X.; Kang, S.; Chen, Z.; Tian, B.; Teo, S. L.; Wang, X.; Chi, X.; Loh, K. P.; Lee, H. W.; Zheng, G. W., Lithium Silicide Surface Enrichment: A Solution to Lithium Metal Battery. *Adv Mater* **2018**, e1801745.

48.   Wan, M.; Kang, S.; Wang, L.; Lee, H. W.; Zheng, G. W.; Cui, Y.; Sun, Y., Mechanical rolling formation of interpenetrated lithium metal/lithium tin alloy foil for ultrahigh-rate battery anode. *Nat Commun* **2020,** *11* (1), 829.

49.   Yao, Y.; Zhao, X.; Razzaq, A. A.; Gu, Y.; Yuan, X.; Shah, R.; Lian, Y.; Lei, J.; Mu, Q.; Ma, Y.; Peng, Y.; Deng, Z.; Liu, Z., Mosaic rGO layers on lithium metal anodes for the effective mediation of lithium plating and stripping. *Journal of Materials Chemistry A* **2019,** *7* (19), 12214-12224.

50.   Qian, J.; Adams, B. D.; Zheng, J.; Xu, W.; Henderson, W. A.; Wang, J.; Bowden, M. E.; Xu, S.; Hu, J.; Zhang, J.-G., Anode-Free Rechargeable Lithium Metal Batteries. *Advanced Functional Materials* **2016,** *26* (39), 7094-7102.

51.   Yan, K.; Lu, Z.; Lee, H.-W.; Xiong, F.; Hsu, P.-C.; Li, Y.; Zhao, J.; Chu, S.; Cui, Y., Selective deposition and stable encapsulation of lithium through heterogeneous seeded growth. *Nature Energy* **2016,** *1* (3), 16010.

52.   Nilsson, V.; Kotronia, A.; Lacey, M.; Edström, K.; Johansson, P., Highly Concentrated LiTFSI–EC Electrolytes for Lithium Metal Batteries. *ACS Applied Energy Materials* **2020,** *3* (1), 200-207.

53.   Nanda, S.; Gupta, A.; Manthiram, A., Anode-Free Full Cells: A Pathway to High-Energy Density Lithium-Metal Batteries. *Advanced Energy Materials* **2020,** *n/a* (n/a), 2000804.